FILTER FAILURE ANALYSIS FOR THE SWAP INSTRUMENT ON BOARD OF PROBA2

Stijn Jonckheere[1], Bart Bergen[1], Bert Pluymers[1], Jean-Philippe Halain[2], Pierre Rochus[2], Wim Desmet[1], Dirk Vandepitte[1]

[1]Department of Mechanical Engineering, K.U. Leuven
Celestijnenlaan 300B – box 2420, B-3001, Heverlee (Leuven), Belgium.
Tel: +32 16 322480; fax: +32 16 322987
e-mail: Stijn.Jonckheere@mech.kuleuven.be

[2] Centre Spatiale de Liège
Avenue Pré Aily, B-4031 Angleur (Liège), Belgium

Keywords: SWAP, PROBA2, optical membranes, vibro-acoustics.

Abstract.   *During its intensive testing campaign, SWAP (Sun Watcher using Active Pixel System detector and image Processing), an optical instrument developed by Centre Spatiale de Liège (CSL) and mounted onto the Belgian satellite PROBA2, was subjected to a multitude of load cases to verify the integrity of the instrument during and after the launch and during the operational phase.*
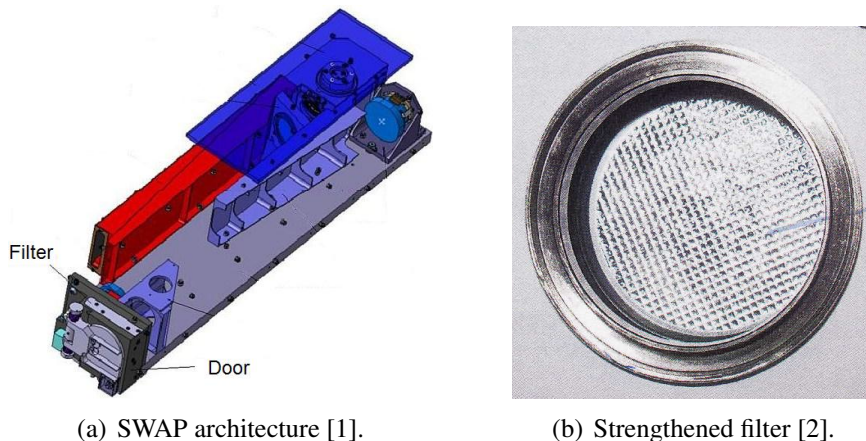
The front and rear filters of SWAP, 200 nm thin films, survived intensive vibration tests on the qualification model and acceptance tests on the flight model, both at an instrument level. During the acoustic test on the spacecraft, the front filter exploded while the rear one was undamaged. A new, strengthened filter, coated with a very fine metal mesh was mounted in the instrument. However, this new filter has less good optical properties due to optical diffraction. Therefore a profound analysis of the filter failure is necessary to provide the best possible optical accuracy for future missions with similar equipment.

Three load cases are further studied in this paper: the acceleration of the rocket, the instrument depressurisation and the vibro-acoustic behaviour under the large sound and vibration levels. The acceleration and depressurisation are studied together in a two-level computational fluid dynamics (CFD) analysis to assess the effect of the venting of the instrument on the differential pressure over the filter. The main focus of this paper is on a numerical vibro-acoustic analysis, following the procedures used by CSL and ESTEC (European Space Research and Technology Centre). This analysis needs special attention because of the presence of a stochastic excitation (diffuse field) and the very nonlinear behaviour of the filter itself due to its small thickness. Also, an additional postprocessing step based on filter displacements, rather than differential pressure, as done in the ESTEC procedure, is discussed.

1

Stijn Jonckheere, Bart Bergen, Bert Pluymers, Jean-Philippe Halain, Pierre Rochus,
Wim Desmet, Dirk Vandepitte

1 INTRODUCTION

On November 2nd 2009 PROBA2[1], the second completely Belgian mini-satellite, produced by the company Verhaert (now QinetiQ), was launched from the ESA-base in Plesetsk, Russia. The goals of the mission were dual: providing a proving ground for new technologies to test their flightworthiness and studying the interaction between the Earth and the Sun and the impact on the so called space weather. One of the scientific instruments on board was the SWAP[2]-instrument, an optical instrument designed by Centre Spatiale de Liège (CSL) to study the solar corona. For this purpose, it is equipped with two optical filters that retain only the frequencies of the solar spectrum relevant to the spaceweather (eUV-frequencies).

The instrument (roughly 50 cm x 15 cm x 10 cm in size) is constructed as is illustrated in Figure 1(a). The instrument cavity is closed, a.o. for cleanliness of the instrument, by a heavy door maintained by a launch lock mechanism with a dedicated labyrinth for depressurisation. Behind that door, which is designed to protect the instrument from acoustic overload, lies a first (small) cavity. Between this small cavity and the large instrument cavity lies the front optical filter, an aluminum membrane with a thickness of 200 nm, which can withstand an ultimate differential pressure of 200 Pa.

(a) SWAP architecture [1].   (b) Strengthened filter [2].

Figure 1: General SWAP architecture and strengthened filter.

The front and rear filters of SWAP survived intensive vibration tests on the qualification model and acceptance tests on the flight model, both at an instrument level. During the acoustic tests of the spacecraft, as in-flight images indicate, the front filter exploded, while the rear one was undamaged. Because of the tight schedule for further testing and launch, the problem had to be dealt with very quickly. Therefore, a new, strengthened filter, coated with a very fine (20 lpi) nickel mesh was mounted (figure 1(b)). This however degrades the optical properties of the filter due to optical diffraction and is therefore not the optimal solution. To learn lessons for future missions, a profound analysis is necessary to assess the true cause of failure for the original filter. A preliminary vibro-acoustic analysis, as performed at ESTEC[3], raised quite some questions. Therefore, CSL proposed to K.U.Leuven to further explore the problem in the context of the master's thesis study [3] of the first author of this paper.

This paper discusses three load cases that can cause filter failure. Apart from the apparent (acoustic) cause of failure in the tests, which was first studied at ESTEC and then at K.U.Leuven

---

[1]Project for Onboard Autonomy 2

[2]Sun Watcher using Active Pixel System Detector and Image Processing

[3]European Space Research and Technology Centre

adopting the ESTEC procedures, the more or less steady-state acceleration of the rocket and the instrument depressurisation, which were tackled by GDTech [4] in a preliminary design study commissioned by CSL, is also discussed.

This acceleration and depressurisation will be studied together in a two-level computational fluid dynamics (CFD) analysis to assess the effect of the venting of the instrument on the differential pressure over the filter.

The main focus of this paper, however, lies on a numerical vibro-acoustic analysis. The analysis needs special attention because of the presence of a stochastic excitation (diffuse sound field), the very nonlinear nature of the filter itself due to its small thickness and the imprecise impact behaviour of the door, which can start flapping and whose acoustic effect is unclear. The procedure followed the same lines as the analysis procedures used by CSL and ESTEC. An additional postprocessing step based on the filter displacements, rather than pressure differences in arbitrary points was added. This approach leads to better, but nevertheless inconclusive results.

The application of these procedures for this type of vibro-acoustic analysis shows that it may in some cases be very hard, or even impossible, to make accurate predictions of the system behaviour when strong nonlinearities are present. Despite the fact that some predictions on the system behaviour can be made in an approximative manner, these predictions have to be used with great care.

2 FLUID DYNAMICS: DEPRESSURISATION AND ACCELERATION

A first important loading on the filter arises from the air escaping the instrument. This so called venting is caused by two effects: the cavity depressurisation and the inertia of the air while the rocket accelerates. These effects are elaborated in the following subsections.

To allow this air to escape smoothly, ventilation labyrinths are put at five distinct locations (see Figure 2(a)). Of these vents, the two utter left on the figure (near the door and just behind the filter) are the most interesting from a filter loading point of view. Since no light is allowed to enter or leave through these ventilation holes (otherwise the instrument would not be able to exclusively study the eUV-spectrum), these vents are engineered as labyrinths (Figure 2(b)). This way, unwanted light is attenuated by means of multiple reflections.

The analyses presented in this section were performed by GDTech [4] in a preliminary study commissioned by CSL. In the analysis, the air was considered to be an ideal gas at 20°C. A preliminary study showed laminar flow in all of the vents.
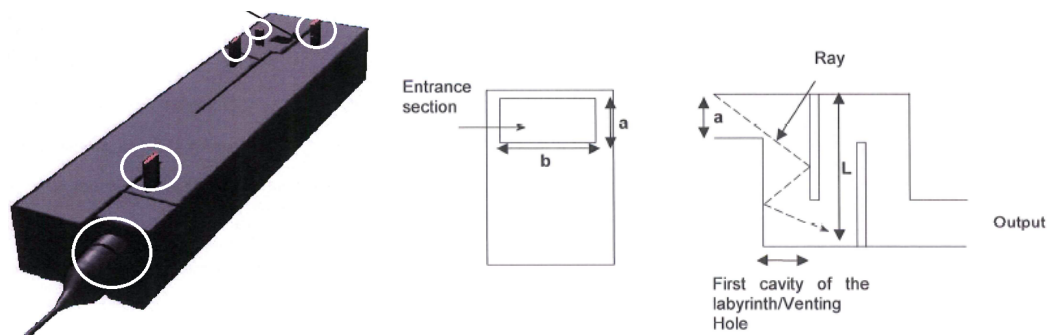
(a) Location of the venting labyrinths [4].

(b) Conceptual drawing of the venting labyrinths [4].

Figure 2: Instrument venting system.

2.1 Depressurisation

Due to the rocket gaining height, the pressure of the instrument environment decreases in time (Figure 3(a)). This causes a pressure difference between the inside and the outside. This creates a flow which is governed by Cauchy's momentum equation.

$$\rho \frac{D\vec{v}}{Dt} = \nabla \cdot (-p\mathbb{I} + \mathbb{T}) \tag{1}$$

with ρ being the fluid density, v the fluid velocity, t the time, p the pressure, $\mathbb{I}$ the identity tensor, $\mathbb{T}$ the fluid stress tensor.

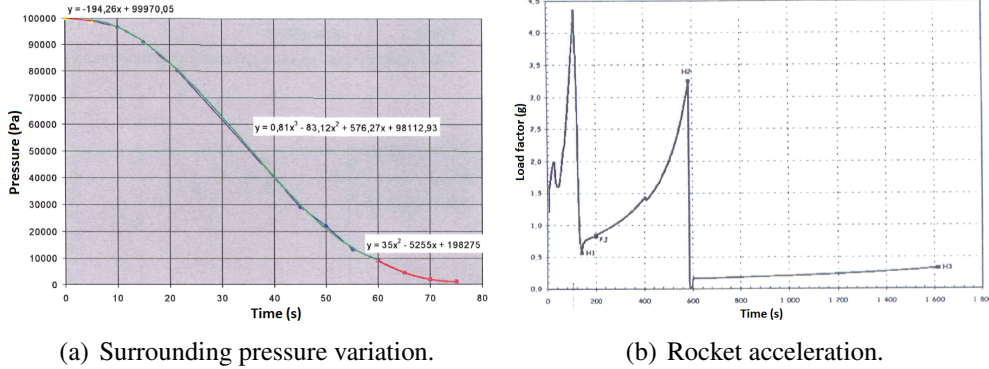(a) Surrounding pressure variation.

(b) Rocket acceleration.

Figure 3: Variation of the imposed loading conditions in time [4].

2.2 Acceleration

The acceleration of the rocket produces a loading on the filter because of the inertia of the air surrounding it. This section will not discuss acceleration effects on the filter itself, which will be quite small because of the very low mass.

The acceleration profile can be found in Figure 3(b). The most penalising situation[4], being a loading perpendicular to the filter, is considered here, for the first eighty seconds.

This inertial loading is introduced into the governing momentum equation (Equation 1) by means of a source term $\rho\vec{a}$, with $\vec{a}$ the rocket acceleration, resulting in:

$$\rho \frac{D\vec{v}}{Dt} = \nabla \cdot (-p\mathbb{I} + \mathbb{T}) + \rho\vec{a} \tag{2}$$

2.3 Analysis

The analysis of the flow effects was performed on two levels: a lower, very detailed level, and a higher, more general one, using approximated results from the lower level.

On the low level we consider the flow inside the venting labyrinths in a detailed 2D CFD analysis (Figures 4(a) and 4(b)).

$$dP_i = aV_{ref} + b\frac{1}{2}\rho_i V_{ref}^2 \tag{3}$$

where a is related to a friction pressure loss (via e.g. the Hagen-Poiseuille equation) and b to a singular pressure drop. This approach was inspired by [5].

---

[4]This is not the true situation.

4

By carrying out CFD calculations for several fluid densities ρ_i, the unknown coefficients a and b can be easily determined.
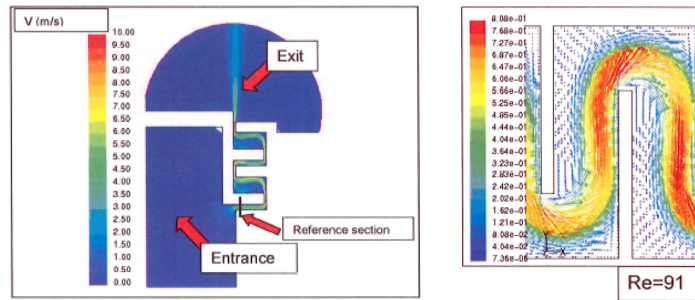
(a) Velocity distribution in the vents.

(b) Detailed view of the velocity distribution.

Figure 4: Detailed 2D velocity distribution in the venting labyrinths [4].

These pressure laws for the different labyrinths are then plugged in a higher-level calculation. This makes it possible to evaluate the pressure difference over the filter caused by the dynamics of the fluid. These results, for the first 80 seconds, are represented in Figure 5.

From this graph it becomes clear that neither the acceleration, nor the depressurisation could be the cause for the failure of the filter. The maximal value for the differential pressure never even comes close to the allowed value of 200 Pa. Other possibilities for the filter failure thus have to be considered.
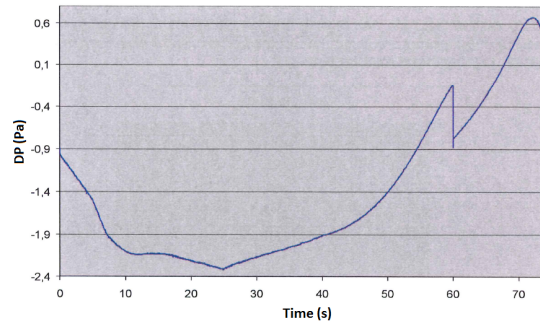

Figure 5: Pressure difference over the filter caused by depressurisation and acceleration effects [4].

3 (VIBRO-)ACOUSTIC ANALYSIS

This section describes the numerical vibro-acoustic analysis that was performed upon the instrument. The focus lies on the acoustic part of the vibro-acoustics, studying the instrument response under the acoustic load caused by the rocket engine. The structural loading was tested extensively by CSL in all types of shaker tests [6]. However, no measurement data of the filter is available for these tests. Visual inspections showed that vibrations alone could not have damaged the filter.

Before discussing this numerical analysis itself, the paper treats the implementation that was used, which differs from standard deterministic vibro-acoustic analyses and the numerical model. Then the (preliminary) results of the analysis itself will be covered. The analysis is concluded with the postprocessing of the acquired results.

3.1 Model

From an initial model, used by CSL for a static structural analysis, the vibro-acoustic system is built by coupling two derived models: a structural model (Figure 6(a)) and an acoustic model (Figure 6(b)).

The structure is modelled using the Finite Element Method (FEM [7]). This procedure discretises the problem domain into nodes and elements. The exact solution within these elements is approximated using simple polynomial shape functions. The application of a weighted residual formulation of the governing differential equation and boundary conditions leads to a system of equations which can be solved for the unknowns, in this case the nodal structural displacements. In a postprocessing step, strains and stresses can then be calculated.

The acoustics are modelled using the Indirect Boundary Element Method (iBEM [8],[9]). This method uses a boundary integral formulation of the governing differential equations. The boundary is discretised into nodes and elements similarly to the FEM. The resulting system of equations is then solved for the unknowns, here acoustic potentials related to pressure and velocity differences across the considered surface. In a next step, the results can be postprocessed to obtain acoustic pressures and velocities anywhere in the field.

Finally, both models are coupled to each other to account for the interaction between structural vibrations and acoustics: structural vibrations impose acoustic normal velocity fields, thus generating pressure waves, while acoustic pressures produce a dynamic loading on the structure. This leads to a vibro-acoustic model in which the structural model (50,000 degrees of freedom) is fully coupled to the acoustic model (20,000 degrees of freedom).

The frequency band for which the models are valid, is determined by the size of the elements. One of the core concepts of the element based methods (FEM and BEM), namely the representation of the dynamic behaviour by polynomial shape functions, limits the frequency range in which these methods are valid. The application of polynomial shape functions introduces two types of numerical errors: interpolation errors, since the dynamic behaviour cannot be exactly covered using polynomials, and pollution errors, caused by a difference between the physical wavelength and the calculated wavelength for the discretised problem. Using the rules of thumb presented in [10],[11], the limiting frequency can be found to be in the structural mesh at 800 Hz. The main acoustic and structural resonances, as well as the highest excitation levels (reaching up to 500 Hz) are located below this frequency. Therefore the mesh is valid in the studied frequency band from 26 to 700 Hz.

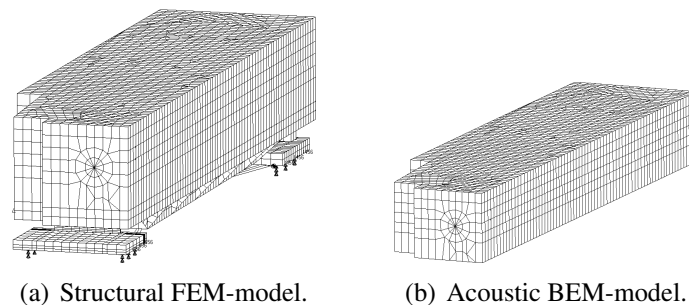(a) Structural FEM-model.   (b) Acoustic BEM-model.
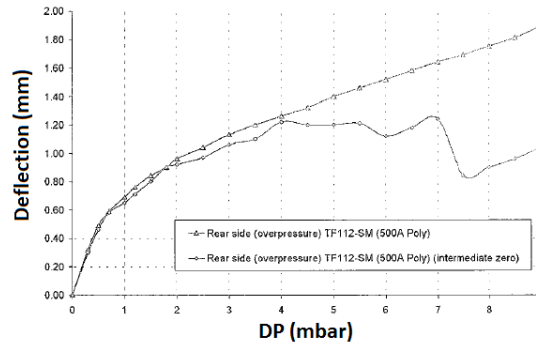
Figure 6: Models for the vibro-acoustic analysis.

Figure 7: Deflection curve of the filter's central point as a function of differential pressure [2].

3.1.1 Sensitivity parameters

A straightforward analysis is impeded by two pronounced nonlinearities in the problem. Firstly there is the complex behaviour of the door. Secondly the nonlinear filter behaviour is discussed.

The complexity of both effects requires the behaviour to be divided into 'extreme' cases. The door will be modelled in a sealed (no more door behaviour as such) and a completely open way (door removed) and the filter in a very flexible and a very rigid way.

Modelling the door A numerical structural analysis shows that the door might not always perfectly close the cavity. This would introduce acoustic leakage and partially expose the filter to the large sound pressure levels. Also, when the door starts 'flapping', repeated impact of the door introduces an additional nonlinearity. Creating an accurate structural model that captures these effects is very difficult. One could create a model based on plate elements that have the kinematic freedom to rotate around a hinge line. The door lock would then be provided by a nodal relationship.

This way of modelling, however, poses serious problems for the acoustics. It is very difficult to impose the correct acoustic boundary conditions since they depend on the degree of structural deformation, which in turn depends on the acoustic behaviour and thus on the acoustic boundary conditions themselves. To account for a possible vibration of the door, two cases are considered. The true situation lies somewhere in between.

1. Door closed: A model with the door completely sealed, thus protecting the filter from any direct exposure to the diffuse sound field.

2. Door open: A model in which the door is completely removed, thus exposing the filter directly to the diffuse sound field.

It is impossible to account for the repeated impact of the door in a steady-state vibro-acoustic analysis. Filter failure caused by this phenomenon will therefore not be detected in the following analysis. This poses an important limitation on the validity of the results and the possible conclusions that can be drawn from it.

Modelling the filter From static deflection tests performed by CSL upon several filter types with and without different protective measures (see.g. Figure 7), it becomes clear that all filters exhibit a very nonlinear behaviour, caused by high membrane forces.

7

With the software that is commercially available, which is aimed at linear vibro-acoustics, it is impossible to create an accurate model that accounts for these membrane forces and that can be plugged into a fully coupled vibro-acoustic analysis. One can however attempt to incorporate these membrane forces into the flexural behaviour by means of a linearisation of the deflection curve, using the well-known analytical expressions for the deflection of a simply supported, circular plate under a uniform differential pressure (Equation 4).

$$w(0) = \Delta p \frac{r_0^4 (5 + \nu)}{64 D (1 + \nu)}$$
$$D = \frac{E t^3}{12(1 - \nu^2)}$$

(4)

In this equation $w(0)$ stands for the deflection of the central point, Δp for the differential pressure, r_0 for the radius of the filter, D for the flexural rigidity, ν for Poisson's ratio, E for the Young's modulus, t for the thickness of the filter.

It is clear from Equation 4 that the flexural rigidity D mainly depends on two parameters: the Young's modulus E and the thickness t. Adjusting the thickness t, however, would not only change the stiffness of the filter, but would also alter the mass. Therefore only the Young's modulus will be varied since this only affects the filter stiffness and not the filter mass.

As a reference, the deflection under a differential pressure of 200 Pa is used. This point is chosen because here the results for a cyclic increase of the differential pressure with intermediate zero difference (○ on Figure 7) and the results for a continuous increase of the differential pressure (△ on Figure 7) start to diverge. This divergence indicates irreversible behaviour and thus filter damage. A calculation based on Equation 4 leads to an equivalent value of the Young's modulus $E_{eq} = 2.30 \cdot 10^9$ GPa. The high value shows the large impact of the membrane forces on the flexural behaviour. The reader should however bear in mind that this is a linearisation around a working point and is thus only exact in that single working point. Also, this altered Young's modulus will lead to a less accurate acoustic behaviour of the filter because by using E_{eq}, the filter is modelled too stiff for small deflections.

For the reasons listed above, two values for the Young's modulus will be studied, one acoustically more correct and the other one more correct from a structural side. The actual situation will again lie somewhere in between.

1. The acoustically more correct $E_{mat} = 70$ GPa, which is standard value for aluminum.

2. The structurally more correct $E_{eq} = 2.30 \cdot 10^9$ GPa (= 2.30 ExaPascal).

3.1.2 Boundary conditions and excitation

Apart from the coupling conditions between the structural and the acoustic model two additional boundary conditions are imposed.

Structural   Both 'feet' of the structural model are clamped at six points (see the arrows on Figure 6(a)). This clamping represents the bolting of the instrument onto the base plate on PROBA2.

Acoustic   For the case of the filter with E_{eq}, the large cavity is locally opened near the filter to retain the acoustic open-closed behaviour. By doing so, a clear image of the deformations and stresses can be created, unlike when using the acoustically more correct E_{mat}, where there are problems due to a very high modal density in the filter (see page 14). The acoustic impact of the ventilation labyrinths, intended to protect the filter from depressurisation effects (see page 3), is neglected in this analysis. Even though low-frequent noise will easily diffract through the labyrinth, and some noise will thus penetrate into the instrument, there will be a lot of reflection in the ducts. Further analyses could incorporate a better estimate for the acoustic admittance of these labyrinths.

The model is acoustically loaded by a diffuse sound field that has the same third octave spectral content and amplitude as the noise generated by the rocket engines.

3.2   Analysis

The following section treats the conducted vibro-acoustic analysis itself and the specific details of the followed implementation.

3.2.1   Implementation

The stochastic nature of the excitation, a diffuse sound field, requires an approach that differs from (standard) deterministic vibro-acoustic analyses. There are different approaches to deal with the stochasticity, like Statistical Energy Analysis (SEA [12]). We are however interested in filter deformations and thus (quasi) deterministic results that indicate whether or not the filter will fail. We therefore need to incorporate the stochastic diffuse field excitation into a deterministic framework. Figure 8 shows the practical implementation of the analysis, which is the way it is implemented in LMS Sysnoise® [13].

From the structural model a modal basis is calculated which contains the mode shapes and modal stresses at the structural resonance frequencies. This modal basis is then imposed on the elements that couple to the acoustic model.

The diffuse field input $X(\omega)$ is decomposed into uncorrelated deterministic excitations $\widetilde{X_i}(\omega)$, in this case plane waves, and their participation factors $q_i(\omega)$ using a Principal Component Analysis [14].

$$X(\omega) = \sum_{i=1}^{n} \widetilde{X_i}(\omega) q_i(\omega) \tag{5}$$

Next, a vibro-acoustic analysis is performed upon the fully coupled structural and acoustic model. A first postprocessing step provides the acoustic power spectral density of the pressure, and the structural power spectral density of the displacements. In the performed analysis a structural modal basis from 0 to 1400 Hz is used, following the rule of thumb to take into account modes with eigenfrequencies up to twice the studied frequency. The diffuse field input is decomposed into 24 uncorrelated plane wave sources.

3.2.2   Analysis

In the vibro-acoustic analysis, as was mentioned earlier (section 3.1.1), four cases are studied: door closed and door open, both for E_{mat} and E_{eq}, based on the procedures followed by CSL and ESTEC.
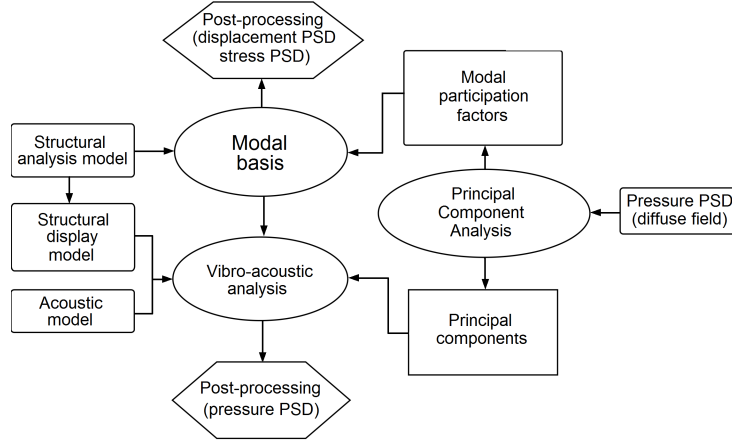
Figure 8: Flow chart of the analysis implementation (based on [15]).

The response is studied in terms of power spectral density of the pressure, in three arbitrary points as defined in Table 1, and the power spectral density of the out-of-plane filter displacements.

Position	Code
1 m outside	□
1 mm in front of filter	×
1 mm behind filter	+

Table 1: Points for Pressure Power Spectral Density.

Door closed   A first set of subcases is based on the assumption that the door perfectly seals the instrument cavity and protects the filter from the harmful sound pressure levels outside. Firstly the purely acoustic behaviour is studied for the cavity as such. Subsequently the vibro-acoustic response is calculated for both E_{mat} and E_{eq}.

Acoustic behaviour   Figure 9(a) shows the frequency response function of pressure in the instrument. The pressure distributions corresponding to the resonances are shown in Figure 9(b). The first (332 Hz) and third resonance (674 Hz) can be related to the analytical case of an acoustically rigid closed box with similar dimensions.

Vibro-acoustic behaviour (E_{mat})   The case with E_{mat} is, as indicated earlier, acoustically closer to reality because of the (usually small) deflections caused by an acoustic field.
    Figure 10(a) shows that the presence of the sealed door gives adequate protection to the filter; the sound levels inside the instrument are much lower than outside. At the higher frequencies, acoustically driven resonances appear, but these don't appear to cause problems.

Vibro-acoustic behaviour (E_{eq}) The case with the equivalent Young's modulus gives a more accurate structural model for high deflections because it attempts to incorporate the effect of the membrane forces into the bending behaviour.
    The (too) rigid filter will however seal the large cavity so that it becomes a closed-closed cavity on its own. This results in the frequency shift of the resonances that is observed when

(a) Frequency response function.

(b) Pressure distribution at selected resonances (from top to bottom: 332-530-674 Hz).
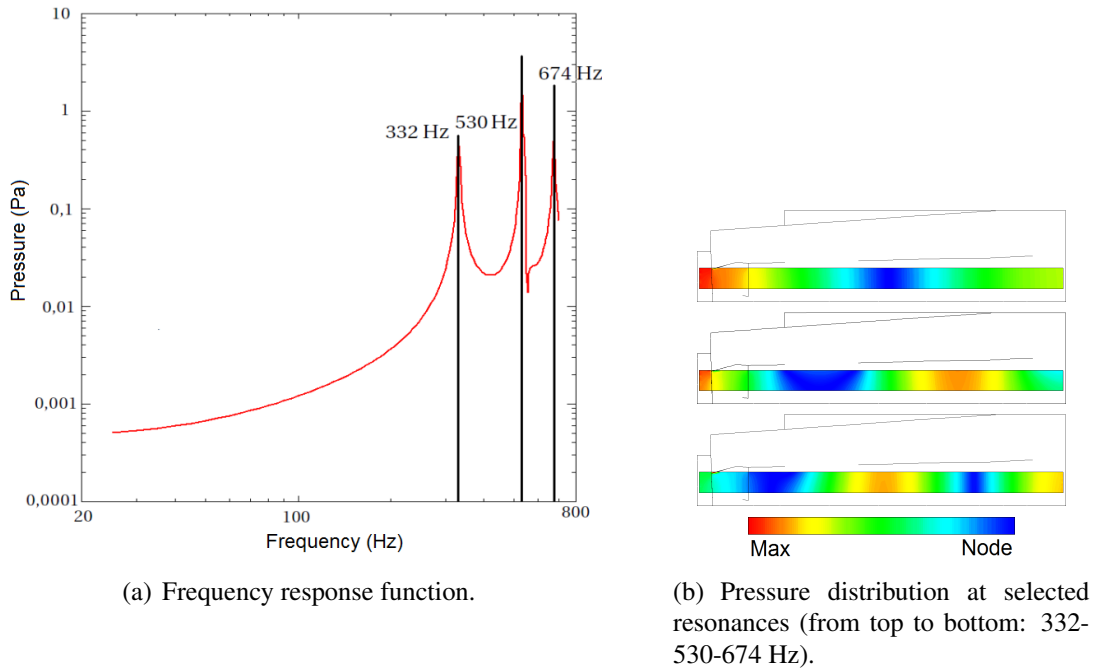
Figure 9: Acoustic behaviour of the cavity with a closed door.

comparing Figure 10(b) to Figure 10(a). The differential pressure appears to stay well below the 200 Pa mentioned on page 8. Following sections (page 12) will however show the relativity of using pressure power spectral data.

Door open   When the door is open, the front of the filter is directly exposed to the diffuse sound field, leading to a large sound level in the small cavity. This produces a large loading on the filter. Similar to the cases with the door closed, firstly the purely acoustic behaviour will be studied and secondly the vibro-acoustic behaviour for both E_{mat} and E_{eq}.

Acoustic behaviour   Figure 11(a) shows the acoustic frequency response function of the instrument. The pressure distributions corresponding to the peaks are shown in figure 11(b). The three resonances (135-398-667 Hz) can all be related to the acoustic modes of an acoustic open-closed box with similar dimensions.

Vibro-acoustic behaviour (E_{mat})   Figure 12(a) shows that for low frequencies the power spectral density of the pressure in front of the filter, as well as behind the filter, follows the sound pressure level outside of the instrument. This is caused by the very low flexural rigidity of the filter which allows the high sound pressure levels in the small cavity in front of the filter to penetrate into the large cavity behind the filter.

Especially at the first two acoustic resonances (135-398 Hz), a considerable differential pressure over the filter may arise.

The location of the resonances corresponds again very well to the purely acoustic case. The resonances are again acoustically driven.

Vibro-acoustic behaviour (E_{eq})   Figure 12(b) shows results that are counterintuitive since we would expect the very rigid filter to practically seal off the instrument cavity.

The differences can be explained by the extra boundary condition that locally opens up the
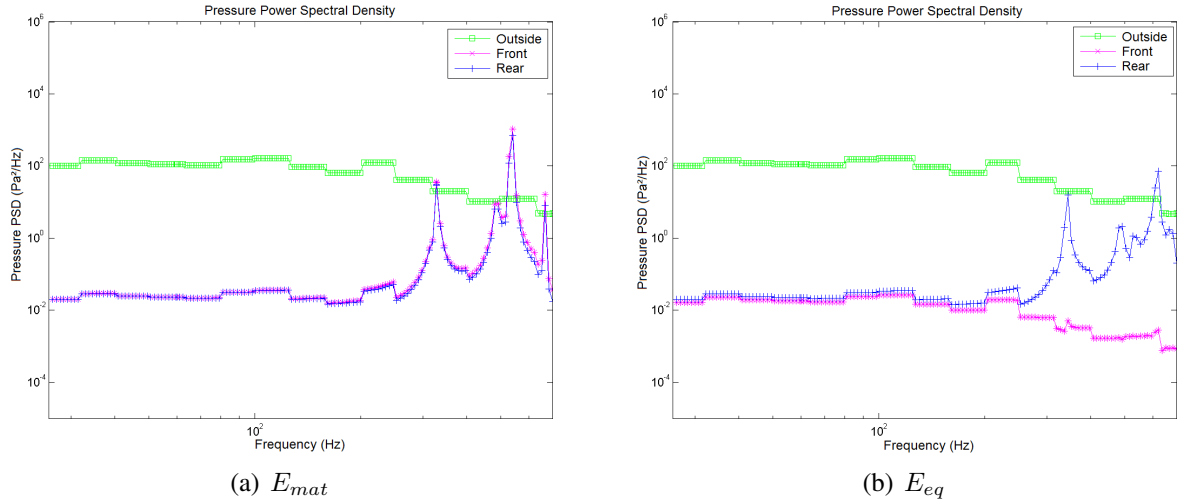
11

(a) E_{mat}

(b) E_{eq}

Figure 10: Power spectral density of the pressure (door closed).

(a) Frequency response function.

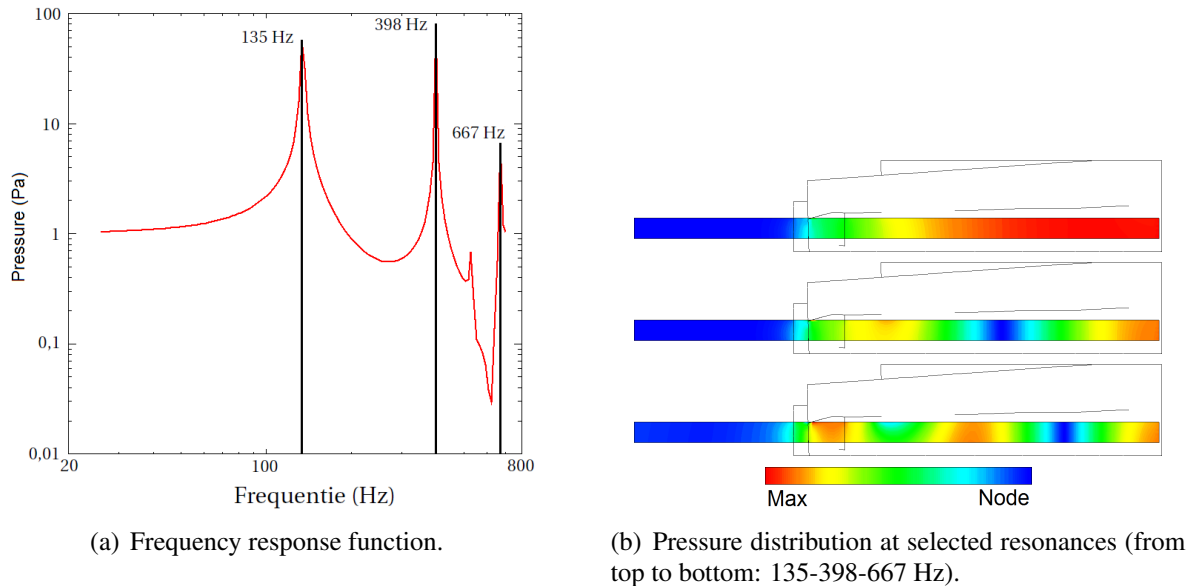(b) Pressure distribution at selected resonances (from top to bottom: 135-398-667 Hz).

Figure 11: Acoustic behaviour of the cavity with the door open.

large cavity, as was discussed on page 8. Without this boundary condition, the results for the point in the rear (+) would be practically indistinguishable from the results on Figure 12(a) since the larger cavity is closed by the very stiff filter, rather than by the door.

3.3 Postprocessing

The power spectral data obtained in the vibro-acoustic analysis can now be used to further assess filter failure and filter failure mechanisms. The practical use of both pressure and displacement data is studied in more detail. Firstly the method using the pressure difference in two arbitrarily chosen points as an estimate of the differential pressure over the filter, as done in the ESTEC procedure, is discussed. Then a more profound approach based on the filter deformation is elaborated.
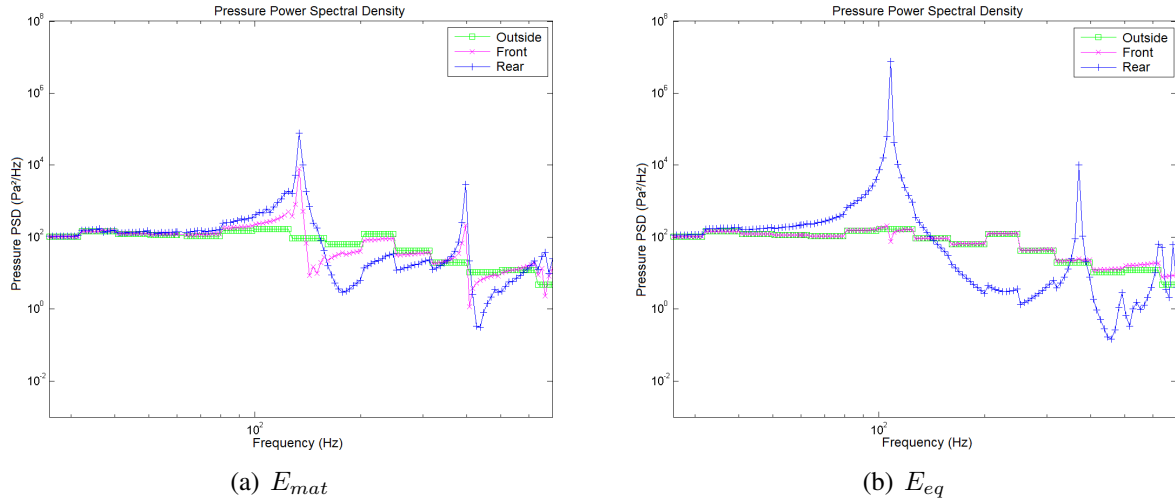
(a) E_{mat}

(b) E_{eq}

Figure 12: Power spectral density of the pressure (door open).

3.3.1 Differential pressure

A first way to assess the loading on the filter is to estimate the differential pressure across the filter. At first sight this differential pressure can be derived, based on the pressure difference between two points, one in front of the filter and one in the rear, as was done earlier (page 9). Moreover, there is experimental data available about the maximal differential pressure the filter can withstand without irreversible deformation or failure (Figure 7), so this variable seems very appealing.

The method has however a major disadvantage that jeopardises its applicability. The results are very sensitive to the estimation for the filter rigidity and the location of the evaluation points. When this rigidity is very low, the main effect that causes a difference between two evaluation points near the filter, is the distance between these points and the mode shapes that govern the response at the given frequencies, rather than the differential pressure over the filter itself. When the rigidity is very high, the filter is acoustically too stiff, and the pressure difference is largely overestimated.

These problems make the interpretation of the results based on the power spectral density of the pressure extremely difficult and even dangerous since it can easily lead to wrong conclusions when the observation points, or the (approximated) filter rigidity are chosen badly. Furthermore this method is not able to show failure mechanisms, it can only (at most) determine whether failure occurs.

3.3.2 Deformations and stresses

A more fundamental way to assess the state of the filter is to look at the deformation of the filter itself by evaluating the displacement of the filter nodes.

Since we model the filter as a plate because no membrane model was available in the software for the vibro-acoustic analysis, and thus not take the membrane behaviour into account, the modal bases for the filter (displacements and stresses) are only partially correct. As a result, it will be impossible to get accurate information on the actual displacements and stresses.

An attempt to ease the problems in a postprocessing step can however be made. By applying (more) appropriate displacement-strain relationships, the distribution of the stresses in the filter

elements can be calculated. This will make it possible to identify possible causes for the filter failure, but it will remain impossible to assess whether or not failure itself will occur.

Constitutive relationships   For a membrane, which exhibits large deflections compared to its thickness, the linearisations made in the plate theory are no longer valid. Higher-order (quadratic) terms also have to be taken into account. Considering these higher-order terms, the displacement-strain relations can, with $\bullet_{i,j} = \frac{\partial \bullet_i}{\partial j}$, be written as [16]

$$\epsilon_{\alpha\beta} = \frac{1}{2}(u_{\alpha,\beta} + u_{\beta,\alpha} + w_{,\alpha}w_{,\beta}) \tag{6}$$

From these equations, the in-plane membrane dispacements u and v can be deleted since all calculations were made with a plate assumption, which has no in-plane deformation, only out-of-plane deformation w. The calculated values do not account in any way for in-plane rigidity. This means no failure mechanisms corresponding to membrane behaviour can be identified. Equation 6 can be rewritten for the different strain components as

$$\epsilon_{xx} = \frac{1}{2}w_{,x}^2 \qquad \epsilon_{yy} = \frac{1}{2}w_{,y}^2 \qquad \gamma_{xy} = w_{,x}w_{,y} \tag{7}$$

Using a proper constitutive relationship, stresses can be calculated from the strains. We assume, because of the small thickness of the membrane, a plane stress situation.

Secondly, an isotropic, linear elastic material is chosen. This is another simplification since failure of the filter is linked with irreversible deformations and thus with plastic behaviour of the material.

These assumptions result in following relationship.

$$\sigma_{ij} = \frac{Et}{(1-\nu^2)} \begin{bmatrix} 1 & \nu & 0 \\ \nu & 1 & 0 \\ 0 & 0 & \frac{1-\nu}{2} \end{bmatrix} \begin{bmatrix} \epsilon_{xx} \\ \epsilon_{yy} \\ \gamma_{xy} \end{bmatrix} \tag{8}$$

For the numerical implementation of this deformation-based postprocessing step, a FEM-procedure was used.

Results E_{mat}   In absence of membrane forces, the filter will have a low flexural rigidity and thus a low flexural eigenfrequency. The filter will exhibit unrealistically large deflections and, in the considered frequency range, a high modal density (Figures 13(a) and 13(b) for the door opened and Figure 14 for the door closed). Because of this high modal density, it is impossible to assess filter stresses. The mesh would need to be drastically refined to be able to calculate the deformations accurately. This is, however, impossible since the calculation time would very strongly increase. But even if this would be feasable, the added value of this refinement is doubtful since the membrane behaviour would still not be incorporated.

When we compare Figure 14 to Figure 13(a), the effect of the closed door on the filter is very clear. The deflection of the filter, and thus its loading, is reduced significantly because of the shielding effect of the door.
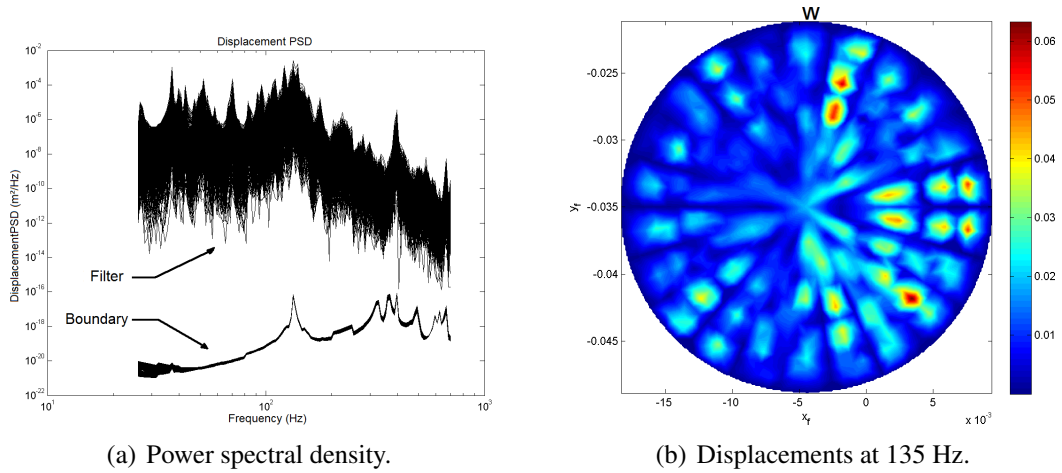
14

(a) Power spectral density.

(b) Displacements at 135 Hz.

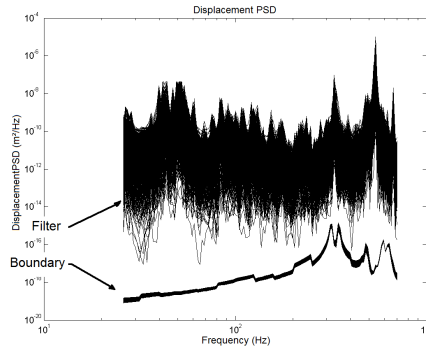Figure 13: Out-of-plane displacements of the filter (door open - E_{mat}).

Figure 14: Power spectral density of the out-of-plane displacements of the filter (door closed - E_{mat}).

Results E_{eq} When the equivalent Young's modulus is used to incorporate the membrane be-haviour, the deflections will be a lot smaller and the high modal density disappears (Figure 15(a) and 15(b)). Therefore the mesh is fine enough to create an accurate image of the deflection and the stresses.

Door open   Because of the extra boundary condition that locally opens the cavity (see page 8), the case with E_{eq} and the door opened, exhibits acoustic open-closed behaviour. In that way, it is possible to look at the deformations in the filter for the acoustically open instrument (Figure 15(b)). This image shows an asymmetric deflection of the filter, caused by the excentric position of the filter with respect to the door opening (thick line in Figure 15(b)). This creates large gradients in the deformations, leading to very local stress peaks (see Figure 16 for von Mises-stresses).

Filter failure may thus be caused by an asymmetry of the door with respect to the filter.

Door closed   The deformation pattern for the case with a closed door (Figure 17(a)) is very different. Because the sound pressure level in the cavity is a lot smaller since the cavity is acoustically closed, the differential pressure over the filter is lower. Also, the filter is modelled very stiff, thus giving low deformations. The global instrument deformations under the diffuse field however, remain relatively unchanged. Therefore Figure 17(b) shows a structural mode of the instrument as a whole, rather than the deflection of the filter. These deformations are thus

15

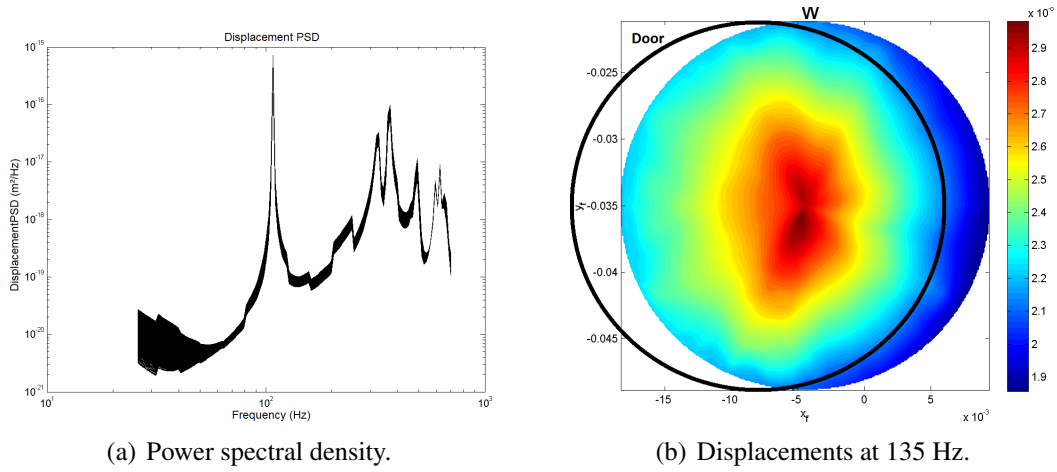of no relevance to the filter loading by cavity acoustics.

(a) Power spectral density.

(b) Displacements at 135 Hz.

Figure 15: Out-of-plane displacements of the filter (door open - E_{eq}).
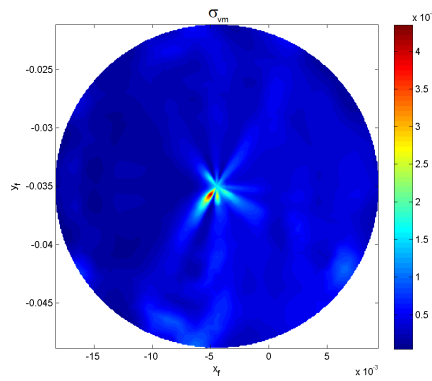
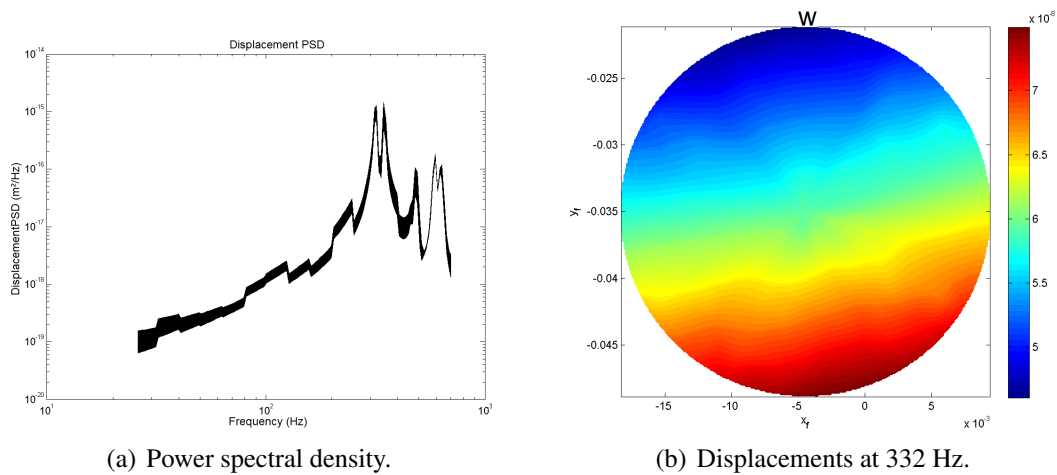Figure 16: von Mises stresses in the filter at 135 Hz (door open - E_{eq}).

(a) Power spectral density.

(b) Displacements at 332 Hz.

Figure 17: Out-of-plane displacements of the filter (door closed - E_{eq}).

16

3.4 Summary

To conclude the discussion of the vibro-acoustic analysis, this section provides a small summary. The reader should however bear in mind the simplifications (Table 2) that were introduced to make a linear vibro-acoustic analysis possible.

Assumption	Cases	Simplification
Door behaviour	Closed and Open	No impact loading Both cases are extremes
Filter model	E_{mat} and E_{eq}	Overestimation stiffness for acoustics E_{eq} is a linearisation
Ventilation labyrinths	–	Vents have no acoustic impact

Table 2: Simplifications and assumptions made.

Door closed   When the door is completely sealed, we have a closed acoustic cavity which is almost completely isolated from the diffuse field loading. The pressures in front and behind the filter (Figure 10) practically coincide and stay at a level well below the level of the diffuse sound field outside. The deformations in the filter are also very low, as Figures 14 and 17 indicate. Although the analysis cannot prove undeniably that the door provides enough protection, because it is difficult to estimate the filter rigidity, it does however show that an acoustically sealing door is a very effective protective measure.

Door open   When the door is removed, the situation changes. The cavity becomes acoustically halfopen and the diffuse field loading can penetrate into the instrument. A substantial pressure difference arises over the filter (Figure 12). It is however difficult to draw conclusions based on this pressure data because of the strong dependency of the results on the studied points. When looking at the more fundamental deformations (Figures 13 and 15), we see that the filter exhibits a substantial deformation. The precise magnitude of this deformation is very hard to predict due to the assumptions (Table 2) made about the filter rigidity, but the (partially) opened door might cause irreversible filter deformation, e.g. by the asymmetric deformation mechanism which was indicated in Figure 15(b).

4   CONCLUSIONS

Several analyses were performed at very different stages of development; in the design stage (CFD analysis), after the testing campaign and even (partially) after the launch of the instrument itself (vibro-acoustic analysis), to check what was the problem that caused a front filter failure, which occured during pre-launch testing.

A CFD analysis was performed by GDTech to assess the effect of the depressurisation and acceleration and the impact of the venting system on the differential pressure over the filter. This analysis was performed on two different levels. Firstly a detailed CFD calculation of the flow through the labyrinths was made and translated to a relation between the entrance velocity and the pressure drop over the labyrinth. These pressure laws were then used in a larger scale analysis to assess the depressurisation of the instrument as a whole. The resulting differential

pressure over the filter is very small and never comes near the allowed value. Filter failure caused by depressurisation is therefore not very likely.

The eventually most probable cause for filter failure was linked with the (vibro-)acoustic behaviour of the instrument cavity, which was studied at ESTEC and later on at K.U.Leuven, following the ESTEC procedures. Though a door was foreseen, a first numerical analysis indicated that this door could start flapping, thus partially opening the acoustic cavity and exposing the filter front to large sound pressure levels. In this way a larger than allowed differential pressure may arise over the front filter. The analysis was, nevertheless, very difficult to do with the currently available commercial software since the optical membrane has a pronounced nonlinear behaviour which cannot be retained entirely in a fully coupled linear vibro-acoustic analysis. Therefore, there is no firm proof that the filter fails indeed due to a mere acoustic overload. Anyhow, the analysis has raised out a plausible cause of this failure (if to be acoustically driven), namely an eccentricity between the door and the filter.

ACKNOWLEDGEMENT

REFERENCES

[1] PROBA2 Science Center, *About SWAP*. `http://proba2.sidc.be/index.html/swap/article/swap-description`, 2010.

[2] J.P. Halain, *Filter Mechanical Characterisation*. Internal CSL report, 2008.

[3] S. Jonckheere, *Vibro-akoestische analyse van het SWAP-instrument aan boord van de PROBA2*, K.U.Leuven, division PMA, Master's thesis, 2010.

[4] Global Design Technology, *SWAP Filter protection study*. Study commissioned by CSL, 2004.

[5] S. Dushman, J.M. Laferty, *Scientific foundations of vacuum technique*. John Wiley & Sons, 1962.

[6] J.S. Servaye, *Vibration test report (SWAP STM)*. Internal CSL report, 2006.

[7] O.C. Zienkiewicz, R.L. Taylor, *The finite element method - The three volume set (6th ed.)*. Butterworth-Heinemann, 2005

[8] C.A. Brebbia, J.C.F. Telles, L.C. Wrobel, *Boundary Element Techniques*. Springer Verlag, 1984.

[9] O. von Estorff, *Boundary elements in acoustics: advances and applications*. WIT, 2000.

[10] S. Marburg, Six elements per wavelength. Is that enough?. *Journal of Computational Acoustics*, **10**, 25–51, 2002.

[11] F. Ihlenburg, I. Babuska, Finite element solution of the Helmholtz equation with high wave number part II: The h-p version of the FEM. *SIAM Journal on Numerical Analysis*, **34(1)**, 315–358, 1997.

[12] R.H. Lyon, R.G. DeJong, *Theory and application of statistical energy analysis (2nd ed.).* Butterworth-Heinemann, 1995.

[13] LMS International, *Sysnoise User manual, Rev. 5.6.*

[14] G.H. Dunteman, *Principal component analysis.* Sage publications, Inc., 1989.

[15] P. Segaert, *Efficient simulation technology for the evaluation of the dynamic response of payloads to diffuse sound field excitation.* `www.aero.org/conferences/sclv/pdfs/segaert_simulation_05.pdf`, 2005.

[16] G.C. Tsiatas, J.T. Katsikadelis, Large deflection analysis of elastic space membranes. *International journal for numerical methods in engineering*, **65**, 264–294, 2006.